

## The physical and chemical properties of the $\rho$ ophiuchi A dense core

YU-CHING CHEN<sup>1,2</sup> AND NAOMI HIRANO<sup>3</sup>

<sup>1</sup>*Department of Astronomy, University of Illinois at Urbana-Champaign, 1002 W. Green Street, Urbana, IL 61801, USA*

<sup>2</sup>*National Center for Supercomputing Applications, University of Illinois at Urbana-Champaign, 1205 West Clark St., Urbana, IL 61801, USA*

<sup>3</sup>*Academia Sinica Institute of Astronomy and Astrophysics, P.O. Box 23-141, Taipei 106, Taiwan*

(Received June 20, 2018; Revised October 5, 2018; Accepted October 17, 2018)

Submitted to ApJ

### ABSTRACT

The physical and chemical properties of the  $\rho$  Ophiuchi A core were studied using 1.3 mm continuum and molecular lines such as C<sup>18</sup>O, C<sup>17</sup>O, CH<sub>3</sub>OH and H<sub>2</sub>CO observed with the Submillimeter Array (SMA). The continuum and C<sup>18</sup>O data were combined with the single-dish data obtained with the IRAM 30m telescope and the James Clerk Maxwell Telescope (JCMT), respectively. The combined 1.3 mm continuum map reveals three major sources, SM1, SM1N and VLA1623 embedded in the extended emission running along the north-south direction, and two additional compact condensations in the continuum ridge connecting SM1 and VLA1623. The spatial distribution of the C<sup>18</sup>O emission is significantly different from that of the continuum emission; the C<sup>18</sup>O emission is enhanced at the eastern and western edges of the continuum ridge, with its peak brightness temperature of 40–50 K. This supports the picture that the  $\rho$ -Oph A core is heated externally from the nearby stars Oph S1 and HD147889. In contrast, the C<sup>18</sup>O intensity is lower than 15–20 K at the center of the ridge where the continuum emission is bright. The C<sup>18</sup>O abundance decreases inside the ridge, and shows anti-correlation with the N<sub>2</sub>H<sup>+</sup> abundance. However, both C<sup>18</sup>O and N<sub>2</sub>H<sup>+</sup> show strong depletion at the Class 0 protostar VLA1623, implying that the dense gas surrounding VLA1623 is colder than the freeze-out temperature of N<sub>2</sub>. The blue- and red-shifted components of CH<sub>3</sub>OH and H<sub>2</sub>CO lines are seen at SM1, suggesting outflow activity of embedded source in SM1, although the spatial distributions do not show clear bipolarity.

*Keywords:* stars: formation - stars: low-mass - submillimeter: ISM - submillimeter: stars

### 1. INTRODUCTION

It is well established that the formation of low-mass stars occurs from the collapse of gravitationally-bound molecular cloud cores (e.g. Shu et al. 1987). Cores before the onset of star formation are called “pre-protostellar cores” or “pre-stellar cores”. Physical and chemical properties of prestellar cores on the verge of star formation are particularly interesting because they provide us the clues to understand the initial conditions of star formation.

The  $\rho$  Ophiuchus cloud complex at a distance of  $137.3 \pm 1.2$  pc (Ortiz-León et al. 2017) is one of the closest molecular clouds with ongoing low-mass star formation. The  $\rho$  Ophiuchus main cloud L1688 consists of several regions labeled from A to F (e.g. Loren et al. 1990); among them, the  $\rho$ -Oph A core is the most prominent core in the millimeter and submillimeter continuum emission (e.g. Motte et al. 1998; Wilson et al. 1999; Johnstone et al. 2000). The

continuum images show that the  $\rho$ -Oph A is a curved ridge consisting of a chain of condensations labeled SM1, SM1N, SM2 and VLA1623. Except VLA1623, which is a widely-studied Class 0 object (Andre et al. 1993), the other condensations in the  $\rho$ -Oph A core have been considered to be starless, because there was no clear signature of star formation. However, recent high resolution and sensitivity observations with the Acatama Large Millimeter/Sub-Millimeter Array (ALMA) at Band 7 have revealed that SM1 contains a spatially compact continuum emission component with a size of  $\sim 40$  AU (Friesen et al. 2014). Friesen et al. (2014) also claimed that SM1 is protostellar because of the X-ray and radio detection toward this source. Later ALMA observations at Band 3 discovered another compact continuum source between SM1 and VLA1623 (Kirk et al. 2017). On the other hand, Nakamura et al. (2012) combined the data obtained with the Submillimeter Array (SMA) and single-dish, and found additional small condensations within SM1. Their results demonstrated the importance of filling the short-spacing data in order to find the small-scale condensations buried in the extended emission.

In order to examine the evolutionary stage of the condensations, kinematic information and chemical properties provided by the molecular line observations are helpful. However, most of the interferometric observations have been limited toward the Class 0 protostar VLA1623 (e.g. [Murillo & Lai 2013](#); [Murillo et al. 2013](#))

In this paper, we present the 1.3 mm continuum and C<sup>18</sup>O (2–1) images obtained with the combination of the SMA and the single-dish data. Our combined images successfully recovered from large-scale to small-scale ( $\sim 5''$ ) emission from the  $\rho$ -Oph A region. We also present the SMA images of the C<sup>17</sup>O, CH<sub>3</sub>OH, and H<sub>2</sub>CO from the SM1 region.

## 2. OBSERVATIONS

### 2.1. SMA data of the $\rho$ -Oph A ridge

The SMA data of the 1.3 mm continuum and the C<sup>18</sup>O (2–1) line were obtained from the SMA data archive. The observations were made on August 5, 2005 in the compact configuration. The primary beam size (FWHM) of the SMA 6-m antennas at 1.3 mm is  $54''$ . The  $\rho$ -Oph A ridge that is prominent in the continuum map (e.g. [Motte et al. 1998](#)) was covered with the 4-pointing mosaic (Figure 1). The spectral correlator that consists of 24 chunks of 104 MHz bandwidth covers 2 GHz bandwidth in each of the two sidebands separated by 10 GHz. The C<sup>18</sup>O line was observed simultaneously with the CO (2–1) and <sup>13</sup>CO (2–1) lines. The spectral resolution of the chunks with the C<sup>18</sup>O and <sup>13</sup>CO lines is 203 kHz per channel, which corresponds to the velocity resolution of  $0.264 \text{ km s}^{-1}$ . The rest of the channels are covered with the uniform resolution of 812 kHz ( $1.048 \text{ km s}^{-1}$ ). The absolute flux density scale was determined from the observations of Callisto and Uranus. A pair of nearby quasars, 1626-298 and 1517-243, were used to calibrate the relative amplitude and phase. The bandpass was calibrated by Jupiter and 3c454.3. The visibility data were calibrated using the MIR package in IDL. The continuum data were obtained by averaging the line-free chunks of both sidebands. To improve the signal-to-noise ratio, the continuum data of the upper and lower sidebands were combined.

### 2.2. Single-dish data

The 1.3 mm continuum data of the  $\rho$ -Oph A region were taken with the IRAM 30m telescope by [Motte et al. \(1998\)](#). The observational details are described in [Motte et al. \(1998\)](#). The continuum image has an effective beam resolution of  $13''$  and 1 sigma noise level of  $\sim 10 \text{ mJy beam}^{-1}$ . The single-dish data of the C<sup>18</sup>O (2–1) line were obtained through the JCMT science archive. The C<sup>18</sup>O observations were conducted on May 3, 1999 using the RxA3 receiver. The backend was a Digital Autocorrelating Spectrometer that was configured to have a spectral resolution of 82.1 kHz ( $0.1067 \text{ km s}^{-1}$ ). The FWHM beam size of the JCMT at a frequency of the C<sup>18</sup>O line is  $22''$ . The  $6' \times 6'$  area including the entire region of the  $\rho$ -Oph A ridge was observed in the on-the-fly mode. The raw data were calibrated and gridded to the data cube using the “ORAC-DR” pipeline ([Cavanagh et al. 2008](#))

in the Starlink software. The resultant rms noise level of the data cube is  $\sim 0.7 \text{ K}$  per channel.

### 2.3. Combining Single-dish and Interferometer data

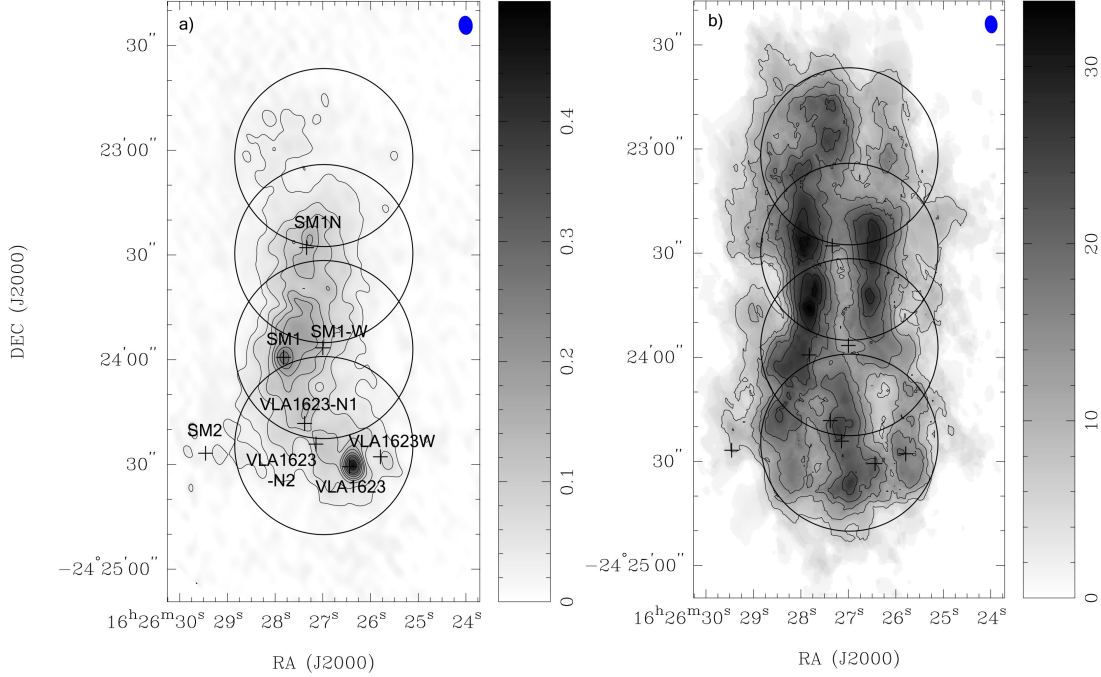
In order to fill the short spacing information that was not sampled by the interferometer, the SMA continuum data were combined with the IRAM 30m data, and the SMA C<sup>18</sup>O data cube were combined with the JCMT data cube. We used the MIRIAD package and followed the procedure described in [Takakuwa \(2003\)](#), which is based on the description of combining single-dish and interferometric data in [Vogel et al. \(1984\)](#). The combined maps were deconvolved using the CLEAN-based algorithm, MOSSDI ([Sault et al. 1996](#)). The synthesized beam is  $5''.2 \times 3''.1$  (P.A. =  $6.1^\circ$ ) for the continuum map and that is  $4''.9 \times 3''.4$  (P.A. =  $6.1^\circ$ ) for the C<sup>18</sup>O map.

### 2.4. The SMA observations toward SM1

The additional SMA observations toward one of the sub-millimeter sources, SM1, were done on Mar. 7 and 9 in 2016 in the compact configuration. The two tracks were conducted with different frequency settings, one including the CH<sub>3</sub>OH ( $5_k-4_k$ ) lines at 241.8 GHz, and the other including the H<sub>2</sub>CO ( $3_{1,2}-2_{1,1}$ ) line at 225.698 GHz, H<sub>2</sub>CO ( $3_{1,3}-2_{1,2}$ ) line at 211.211 GHz and C<sup>17</sup>O (2–1) line at 224.714 GHz. The 4 GHz bandwidth in each sideband was covered by 48 chunks of 104 MHz bandwidth. The spectral resolution of the chunks with the CH<sub>3</sub>OH, H<sub>2</sub>CO, and C<sup>17</sup>O lines was 204 kHz ( $0.264 \text{ km s}^{-1}$ ) per channel. The bright quasar, 3c273, was observed as a bandpass calibrator, and the nearby quasar, 1517-243, was used as phase and amplitude calibrators. The flux calibrators of the first track were Callisto and Ganymede, and those of the second track were Europa and MWC349A. The visibility data were calibrated using the MIR package, and imaged using the MIRIAD package. The synthesized beam sizes are  $3''.3 \times 2''.4$  for the CH<sub>3</sub>OH data cube,  $4''.0 \times 2''.7$  for the H<sub>2</sub>CO ( $3_{1,3}-2_{1,2}$ ) data cube,  $3''.3 \times 2''.4$  for the H<sub>2</sub>CO ( $3_{1,2}-2_{1,1}$ ) data cube and  $3''.7 \times 2''.5$  for C<sup>17</sup>O data cube. The  $1\sigma$  rms noise level is  $\sim 0.09 \text{ Jy beam}^{-1}$  per channel in CH<sub>3</sub>OH and H<sub>2</sub>CO data cube, and that of the C<sup>17</sup>O data cube is  $\sim 0.07 \text{ Jy beam}^{-1}$ . Only the two CH<sub>3</sub>OH lines with the lowest energy levels ( $5_0-4_0 \text{ A}$ ,  $E_{\text{up}} = 34.8 \text{ K}$  and  $5_{-1}-4_{-1} \text{ E}$ ,  $E_{\text{up}} = 40.4 \text{ K}$ ) were detected. Both H<sub>2</sub>CO lines ( $3_{1,3}-2_{1,2}$ ,  $E_{\text{up}} = 32.1 \text{ K}$  and  $3_{1,2}-2_{1,1}$ ,  $E_{\text{up}} = 33.4 \text{ K}$ ) were detected in the SMA observations, but we only present the H<sub>2</sub>CO ( $3_{1,3}-2_{1,2}$ ) line, since the lines having similar energy levels show similar structures. The continuum data were obtained by averaging the line-free chunks of both sidebands. The data of two sidebands were combined in order to improve the signal-to-noise ratio. In addition, the continuum visibility data of the two tracks are also combined. The synthesized beam and the  $1\sigma$  rms noise level of the continuum map are  $3''.9 \times 2''.9$  (P.A. =  $-9.1^\circ$ ) and  $2.7 \text{ mJy beam}^{-1}$ , respectively.

## 3. RESULTS AND ANALYSIS

### 3.1. 1.3 mm continuum



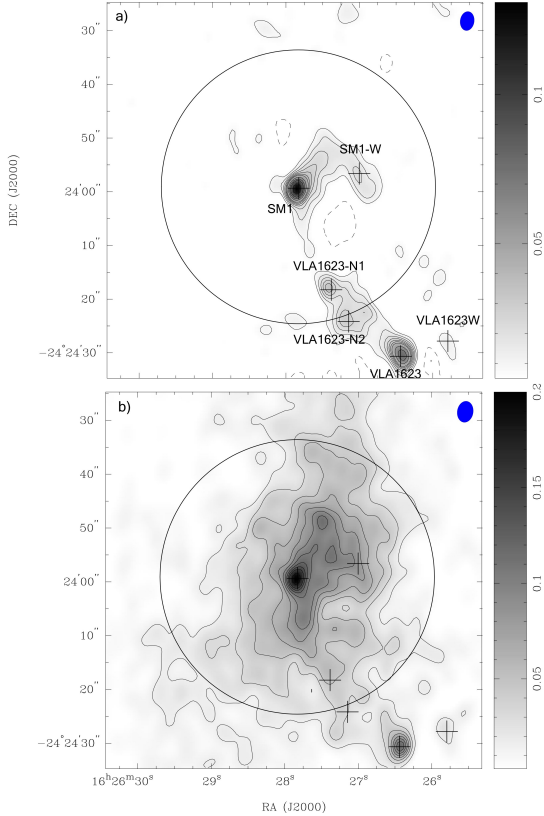
**Figure 1.** (a) 1.3 mm Continuum map obtained by combining the IRAM 30m data and the SMA data of 4-pointing mosaic. The  $1\sigma$  rms noise level of the map is  $8.5 \text{ mJy beam}^{-1}$ . Solid contours denote 30, 60, 90, 120, 150, 200, 250, 300 and  $400 \text{ mJy beam}^{-1}$ . Gray scale starts from 0 to  $470 \text{ mJy beam}^{-1}$ . The cross signs except SM2 and SM1N are the 1.3 mm peak determined from the maps presented in Figure 2. The locations of SM2 and SM1N are from Motte et al. (1998). The ellipse at top right corner denotes the beam size of  $5''.2 \times 3''.7$ . Solid circles denote the field of views of the SMA in four pointing mosaic observations. (b)  $\text{C}^{18}\text{O}$  (2–1) integrated intensity map derived from JCMT 15m telescope and the SMA data. The  $1\sigma$  rms noise level of the map is  $2.1 \text{ Jy beam}^{-1} \text{ km s}^{-1}$ . Solid contours denote  $3, 5, 7, 9, 11, 13$  and  $15 \times 1\sigma$  rms level. The range of the gray scale is  $0\text{--}33.7 \text{ Jy beam}^{-1} \text{ km s}^{-1}$ . The ellipse at top right corner denotes the beam size of  $4''.9 \times 3''.4$ .

Figure 1a shows the 1.3 mm continuum emission from  $\rho$ -Oph A region obtained by the combination of the IRAM 30m data and the SMA interferometer data. The continuum emission shows the N-S ridge similar to the single-dish map presented in Mezger et al. (1992), Andre et al. (1993) and Motte et al. (1998). There are three major components, VLA1623, SM1, and SM1N. Our high resolution map having an angular resolution of  $\sim 5''$  reveals that each source has internal structure. The brightest source in this region is VLA1623, a well-studied class 0 protostar (e.g. Andre et al. 1993). The recent studies by Murillo & Lai (2013) and Chen et al. (2013) showed that VLA1623 consists of three sources, VLA1623A, B and W, which are suggested to be a triple non-coeval system. In our continuum map, VLA1623A and B, having a separation of  $\sim 1''$ , are not spatially resolved. On the other hand, VLA1623W is identified as a separate peak.

The emission from the second brightest source, SM1, shows a well-defined peak. Recent ALMA observations at 359 GHz (Friesen et al. 2014) have revealed that this source is very compact, having a size of only  $0.31''$  ( $\sim 42 \text{ au}$  at 137 pc). The compact source is surrounded by the extended structure having an elongation toward the north-western direction. In the SM1 region, Nakamura et al. (2012) reported three condensations. The brightest one, a1, corresponds to the continuum peak of our map. The other two, a2 and a3, are not clearly seen in our map, probably because of the low inten-

sity contrast of these components and the lower angular resolution of our map. VLA1623 and SM1 are connected by the curved emission ridge, having two local peaks labeled as VLA1623-N1 and N2. In contrast to SM1 and VLA1623, the northern source SM1N is spatially extended and contains no compact component, which is consistent with the 359 GHz results of Friesen et al. (2014). The emission from SM2 is less significant, because this source is located beyond the area covered by our 4-pointing mosaic. The 3mm continuum map in Kirk et al. (2017) have the similar structure as our continuum map; both the extended filament around north-east of SM1 and VLA1623-N1 and N2 are clearly seen in their map.

Figure 2a shows the continuum map of the SM1 region observed with the SMA in 2016. With higher sensitivity thanks to the wider bandwidth, two sources, VLA1623-N1 and N2, are clearly seen in this map. The SMA data are also combined with the IRAM 30m data (Figure 2b) The combined map recovers well the extended emission around the SM1 peak. The continuum emission extends to the north of SM1, which is consistent with the 340 GHz results of Nakamura et al. (2012). However, the small scale condensations a2 and a3 reported by Nakamura et al. (2012) are not clearly seen in our maps. Instead, our SMA map shows the local intensity maximum to the west of SM1, which is labeled as SM1-W. Instead of being obvious in the SMA map (Figure 2a), VLA1623-N1, -N2 and SM1-W are not significant in the



**Figure 2.** (a) The SMA map of the 1.3 mm continuum centered at SM1. The  $1\sigma$  rms noise level is  $2.7 \text{ mJy beam}^{-1}$ . The solid contours denote 3, 5, 7, 9, 11, 13, 15, 20, 25, 30, 40 and  $50 \times 1\sigma$  level, while the dashed contour denotes  $-3\sigma$  levels. The gray scale ranges from 5 to  $131 \text{ mJy beam}^{-1}$ . The ellipse at the top right denotes the synthesized beam of  $3''.5 \times 2''.5$ . Solid circle denotes the field of view of the SMA. (b) The SMA + IRAM 30m map of the 1.3 mm continuum centered at SM1. The  $1\sigma$  rms noise level of the map is  $3 \text{ mJy beam}^{-1}$ . Solid contour denote 5, 10, 15, 20, 25, 30, 35, 40, 45, 50, 60, 70, 80 and  $90 \times 1\sigma$  level. The gray scale ranges from 5 to  $200 \text{ mJy beam}^{-1}$ . The ellipse at top right corner denotes the synthesized beam of  $3''.9 \times 2''.9$ . The cross signs denote the continuum peaks derived from the Gaussian fitting.

combined map (Figure 2b) because of the rather high-level emission from the extended component.

The coordinates, peak flux density, total flux, size, and position angle of each source were determined from the single Gaussian component fitting using the MIRIAD task IMFIT. The size and position angle of each source are derived after deconvolved with the beam. The parameters of VLA1623-N1, -N2 and SM1-W are derived from the SMA map shown in Figure 2a, while those of VLA1623, VLA1623W, and SM1 are from the combined map shown in Figure 2b. The derived parameters are listed in Table 1.

### 3.2. $\text{C}^{18}\text{O}$ (2-1)

The integrated intensity map of the  $\text{C}^{18}\text{O}$  obtained by combining the JCMT data and the SMA data is presented in Fig-

ure 1b. Although the  $\text{C}^{18}\text{O}$  emission comes from the N-S ridge of the  $\rho$ -Oph A, its spatial distribution is significantly different from that of the continuum; the  $\text{C}^{18}\text{O}$  emission is bright in the eastern and western edges of the ridge, and rather faint at the center of the ridge where the continuum emission is bright.

In the northern part, the anti-correlation between the  $\text{C}^{18}\text{O}$  and continuum is significant; the continuum peak SM1N is located between two bright ridges of the  $\text{C}^{18}\text{O}$ . In the southern part, there is a third ridge of  $\text{C}^{18}\text{O}$  emission connecting SM1 and VLA1623. However, the  $\text{C}^{18}\text{O}$  does not follow the curved ridge traced by the 1.3 mm continuum. In addition, locations of the  $\text{C}^{18}\text{O}$  peaks do not coincide with the continuum peaks. On the other hand, the  $\text{C}^{18}\text{O}$  peak coincides with the continuum peak at VLA1623W.

Since our  $\text{C}^{18}\text{O}$  map contains the short-spacing information obtained with the JCMT, the lack of bright emission at the center of the ridge is not the effect of spatial filtering of the interferometer. The CO and  $^{13}\text{CO}$  lines observed in the  $\rho$ -Oph molecular cloud often show the self-reversal line profile, which could produce intensity drop at the line of sight at high optical depth. However, the observed  $\text{C}^{18}\text{O}$  line does not show such a self-reversal profile. Such an anti-correlation between the  $\text{C}^{18}\text{O}$  and continuum was not clear in the previous single-dish observations (Liseau et al. 2010; White et al. 2015) due to their angular resolutions. Recently, Liseau et al. (2015) deconvolved their  $\text{C}^{18}\text{O}$  (3-2) image, and improved the angular resolution from  $19''$  to  $7''$ . Their deconvolved  $\text{C}^{18}\text{O}$  image also reveals the anti-correlation with the continuum distribution. Moreover, by comparing our  $\text{C}^{18}\text{O}$  integrated intensity map with the  $\text{N}_2\text{H}^+$  map from Di Francesco et al. (2004), we found that the most of the  $\text{N}_2\text{H}^+$  emission comes from the region between two  $\text{C}^{18}\text{O}$  ridges (Figure 3). The highest  $\text{N}_2\text{H}^+$  emission occurs across SM1N and SM1, where the  $\text{C}^{18}\text{O}$  emission is missing. The spatial distribution of the  $\text{C}^{18}\text{O}$  is anti-correlated with that of  $\text{N}_2\text{H}^+$  except the southern ridge including VLA1623-N1 and VLA1623-N2.

The  $\text{C}^{18}\text{O}$  peak intensity map shown in figure 4 indicates that the prominent  $\text{C}^{18}\text{O}$  ridges have high brightness temperature of  $>40 \text{ K}$ ; whereas, in the rest region, the temperature is roughly  $25 \text{ K}$  or below. A notable thing is that, except SM1, where the temperature is roughly  $40 \text{ K}$ , major dust condensations are located in the regions with lower brightness temperature; VLA1623-N1 and VLA1623-N2 are in the region with  $\sim 30 \text{ K}$ , and SM1N, VLA1623, and VLA1623W are in the regions of  $\sim 25 \text{ K}$ .

The channel map (Figure 5) and the position-velocity map along the N-S cut through R.A. =  $16^{\text{h}}26^{\text{m}}27^{\text{s}}$  (Figure 6) show that there is a significant velocity gradient along the  $\rho$ -Oph A ridge. The velocity centroid in the northern part of the ridge is at  $V_{\text{LSR}} \sim 3.1 \text{ km s}^{-1}$ , and gradually changes to  $\sim 3.7 \text{ km s}^{-1}$  at the position of SM1, which is consistent with the  $\text{C}^{18}\text{O}$  (3-2) results of Liseau et al. (2010). The southern redshifted component shows an arc-like feature at  $\sim 4.3 \text{ km s}^{-1}$ . This arc-like feature follows the eastern edge of the continuum arc connecting SM1 and VLA1623 (see Panel 10 of Figure 5). Bergman et al. (2011) have also shown that the

**Table 1.** The fitting parameters of each submillimeter source

Source	R.A. (J2000)	Dec. (J2000)	$S_p$ (Jy beam $^{-1}$ )	$S_t$ (Jy)	FWHM (arcsec)	P.A. (degrees)	Mass <sup>a</sup> ( $M_\odot$ )	$M_{BE}$ ( $M_\odot$ )
VLA1623	16:26:26.44	-24:24:30.65	0.50	0.86	3''2×2''4	7.3	0.41	0.010
VLA1623-N1*	16:26:27.38	-24:24:18.26	0.049	0.11	4''7×1''8	44.3	0.05	0.014
VLA1623-N2*	16:26:27.15	-24:24:24.17	0.06	0.31	6''8×5''3	60.1	0.15	0.02
VLA1623W	16:26:25.80	-24:24:27.81	0.14	0.32	5''5×2''4	14.4	0.15	0.017
SM1	16:26:27.83	-24:23:59.34	0.19	0.59	5''8×4''2	-9.3	0.28	0.018
SM1-W*	16:26:27.00	-24:23:56.61	0.02	0.17	12''2×4''0	36.4	0.08	0.038

\*The parameters for VLA1623-N1, VLA1623-N2 and SM1-W are determined from the SMA map (Figure 2a) only.

<sup>a</sup> The uncertainty in the mass calculation derived from the  $1\sigma$  error in the measured flux is  $\sim 10\%$ .

**Table 2.** The column density and abundance of each submillimeter source

Source	$N_{H_2}$ ( $10^{23}\text{cm}^{-2}$ )	$N_{C^{18}O}$ ( $10^{16}\text{cm}^{-2}$ )	$N_{N_2H^+}$ ( $10^{12}\text{cm}^{-2}$ )	$X_{C^{18}O}$ ( $10^{-8}$ )	$X_{N_2H^+}$ ( $10^{-11}$ )	$X_{C^{17}O-SMA}$ ( $10^{-9}$ )	$X_{C^{18}O-SMA}$ ( $10^{-8}$ )
VLA1623	5.8	2.5	7.8	4.3	1.4	3.6 <sup>b</sup>	1.3 <sup>c</sup>
VLA1623-N1	2.7	5.2	54.2	24.4	20.2	2.4 <sup>b</sup>	0.88 <sup>c</sup>
VLA1623-N2	2.4	4.5	60.1	18.8	25.1	6.0 <sup>b</sup>	2.2 <sup>c</sup>
VLA1623W	1.5	2.1	< 6 <sup>a</sup>	14.2	< 3.9 <sup>a</sup>	< 1.7 <sup>ab</sup>	< 0.62 <sup>c</sup>
SM1	5.4	10.2	17.0	19.1	3.2	2.4 <sup>b</sup>	0.88 <sup>c</sup>
SM1-W	2.2	6.6	65.5	3.8	20.5	< 5.2 <sup>ab</sup>	< 1.9 <sup>c</sup>

<sup>a</sup>The flux of the  $N_2H^+(C^{17}O)$  emission is below the  $3\sigma$  noise level.

<sup>b</sup>The  $C^{17}O$  abundance is calculated from the SMA data only.

<sup>c</sup>The  $C^{18}O$  abundance is derived by multiplying the  $C^{17}O$  abundance estimated from the SMA data by the  $^{18}O/^{17}O$  abundance ratio, 3.65 (Penzias 1981).

chemical properties are different between the northern part and southern part of the ridge. The deuterated species like HDCO,  $D_2CO$  and  $N_2D^+$  are abundant in the southern part with  $V_{LSR} \sim 3.7 \text{ km s}^{-1}$ , but are deficient in the northern part with  $V_{LSR} \sim 3.1 \text{ km s}^{-1}$ .

The abrupt velocity change near SM1N in moment 1 map (Figure 7) is likely to be originated from the third component at  $V_{LSR} \sim 2.9 \text{ km s}^{-1}$ , which is clearly seen in the  $H_2CO$  position-velocity and profile maps in Bergman et al. (2011). This component is not clearly seen in the position-velocity map of  $C^{18}O$  (3–2) in Bergman et al. (2011), while clearly seen in our  $C^{18}O$  (2–1) position-velocity map. Furthermore, the  $2.9 \text{ km s}^{-1}$  component has the C-shaped pattern seen in the mom1 map and channel map, and might be related to the methanol rich gas, which also shows C-shaped morphology in larger scale (Bergman et al. 2011; Garay et al.

2002). Overall, it is likely that the  $\rho$ -Oph A ridge consists of three components with different velocities and chemical properties; the northern component at  $3.1 \text{ km s}^{-1}$  which is deficient in deuterated species, the southern deuterium-rich component at  $3.7 \text{ km s}^{-1}$ , and the north-western component at  $2.9 \text{ km s}^{-1}$  having high methanol abundance.

### 3.3. $C^{18}O$ and $N_2H^+$ Abundance

The column density of  $H_2$  in  $\rho$ -Oph A can be determined from 1.3 mm continuum emission by the formula

$$N(H_2) = \frac{S_\nu}{\Omega_m \mu m_H \kappa_\nu B_\nu(T_{\text{dust}})} \quad (1)$$

where  $S_\nu$  is the 1.3 mm flux density,  $\Omega_m$  is the solid angle of the beam,  $\mu$  is the mean molecular weight,  $m_H$  is the mass of the atomic hydrogen,  $\kappa_\nu$  is the dust opacity per unit mass.

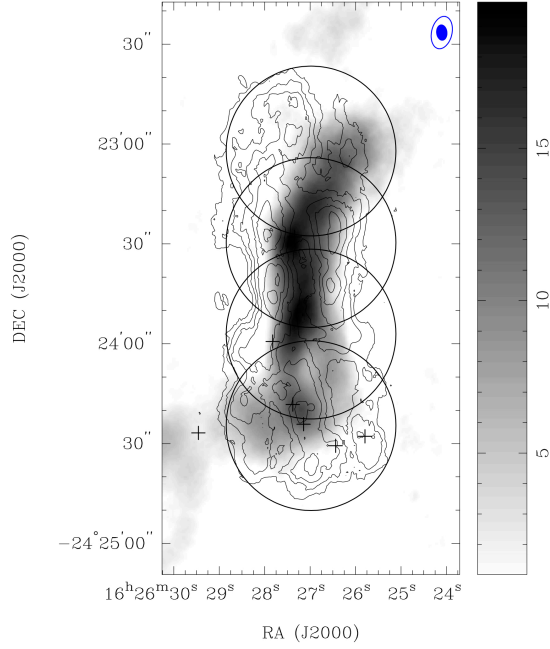


**Figure 3.** A comparison between  $\text{C}^{18}\text{O}$  (contours) and  $\text{N}_2\text{H}^+$  (gray scale) integrated intensity maps. The  $\text{N}_2\text{H}^+$  map is obtained from Di Francesco et al. (2004). The rms noise level, contours and resolution of the  $\text{C}^{18}\text{O}$  map are the same as in Figure 1b. For the  $\text{N}_2\text{H}^+$  map, the  $1\sigma$  rms noise level is  $1.0 \text{ Jy beam}^{-1} \text{ km s}^{-1}$  and the gray scale ranges from  $1.0$  to  $19.8 \text{ Jy beam}^{-1} \text{ km s}^{-1}$ . The hollow ellipse at the top right corner denotes the beam size of the  $\text{N}_2\text{H}^+$  map,  $9'.9 \times 6'.2$ .

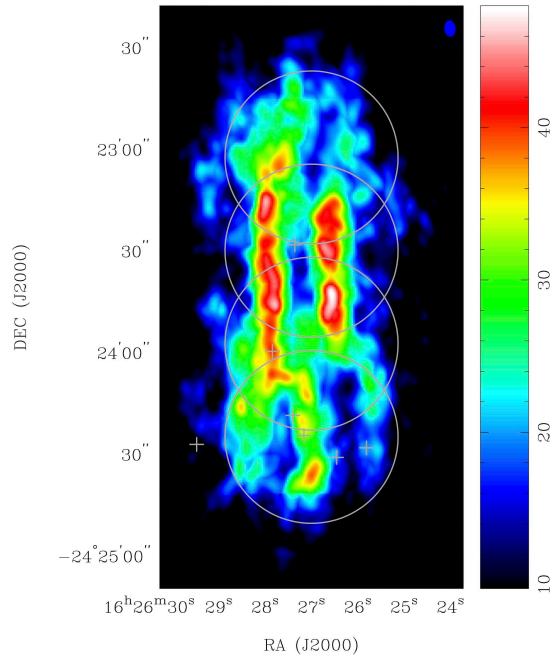


**Figure 4.** The peak intensity map of the  $\text{C}^{18}\text{O}$  in the  $\rho$ -Oph A ridge. The color scale ranges from 10 K to 48 K. The resolution and cross symbols are the same as those in Figure 1b.

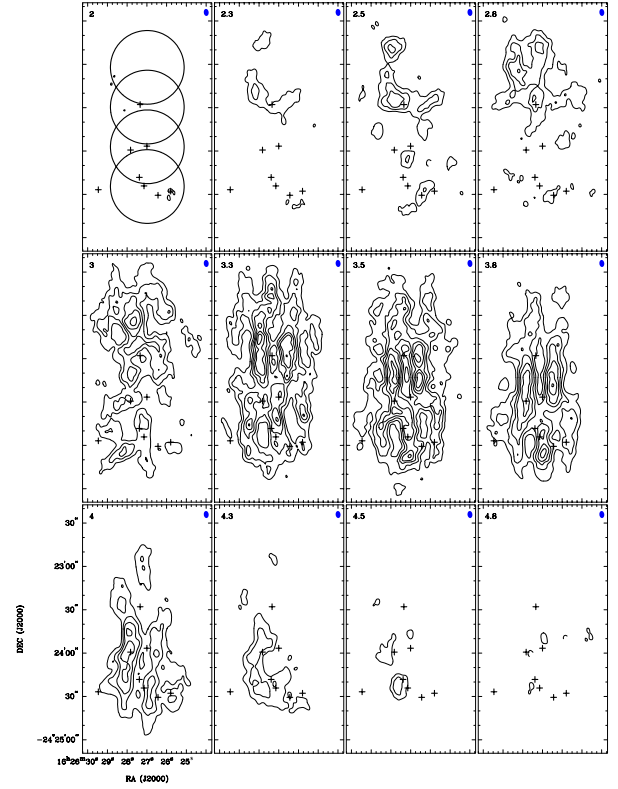


**Figure 5.** Velocity-channel maps of the  $\text{C}^{18}\text{O}$ .  $1\sigma$  rms noise level of the map is  $2.1 \text{ Jy beam}^{-1}$ . The solid contours denote  $3, 5, 7, 9, 11$  and  $13 \times 1\sigma$  level, while the dashed contour denotes  $-3\sigma$  level. The resolution and cross symbols are the same as those in Figure 1b.

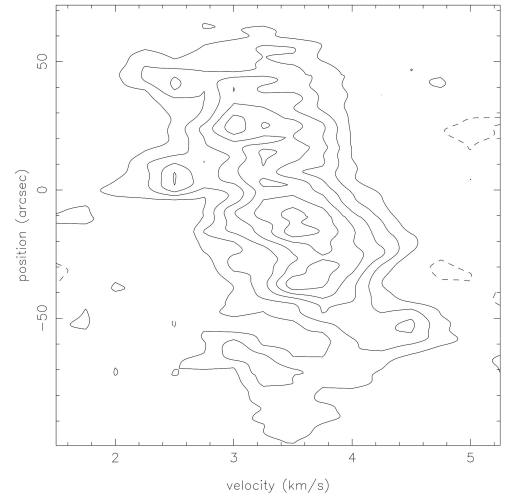


**Figure 6.** Position-Velocity diagram of the  $\text{C}^{18}\text{O}$  along the N-S direction centered at R.A.=  $16:26:26.98$  and Dec= $-24:23:29.60$ . The solid contours denote  $4.32, 8.64, 13.0, 17.3, 21.6, 25.9 \text{ Jy beam}^{-1}$ .

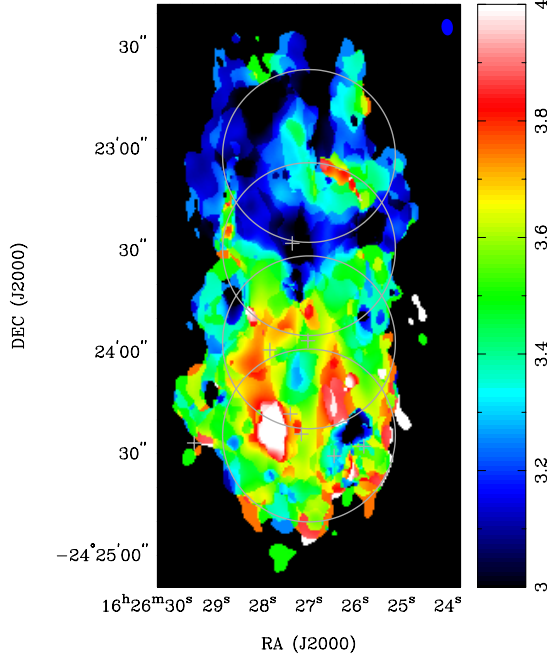


**Figure 7.** The velocity centroid (moment 1) map of the  $C^{18}O$  in the  $\rho$ -Oph A ridge. The color scale ranges from  $V_{LSR} = 3 \text{ km s}^{-1}$  to  $4 \text{ km s}^{-1}$ . The resolution and cross symbols are the same as those in Figure 1b.

(assumed to be  $0.005 \text{ cm}^2 \text{ g}^{-1}$ , which is the same value used by Motte et al. (1998) for pre-stellar clumps and cores), and  $B_{\nu}(T_{\text{dust}})$  is the Planck function at the dust temperature, which is assumed to be 27 K (Andre et al. 1993).

On the other hand, by following Mangum & Shirley (2015), the  $C^{18}O$  and  $N_2H^+$  column densities can be derived from the local thermodynamic equilibrium (LTE) assumptions,

$$N(C^{18}O) = \frac{3.15 \times 10^{15}}{\theta_a(\prime)\theta_b(\prime)} \left( \frac{\tau}{1 - e^{-\tau}} \right) \frac{\exp\left(\frac{15.8}{T_{\text{ex}}}\right)}{\exp\left(\frac{10.54}{T_{\text{ex}}}\right) - 1} \times \left( \frac{T_{\text{ex}} + 0.88}{T_{\text{ex}} - 2.73} \right) \int S_{\nu}(\text{Jy}) dv (\text{kms}^{-1}) \text{ cm}^{-2} \quad (2)$$

and,

$$N(N_2H^+) = \frac{4.48 \times 10^{13}}{\frac{1}{9}\theta_a(\prime)\theta_b(\prime)} \left( \frac{\tau}{1 - e^{-\tau}} \right) \frac{\exp\left(\frac{4.47}{T_{\text{ex}}}\right)}{\exp\left(\frac{4.47}{T_{\text{ex}}}\right) - 1} \times \left( \frac{T_{\text{ex}} + 0.75}{T_{\text{ex}} - 2.73} \right) \int S_{\nu}(\text{Jy}) dv (\text{km s}^{-1}) \text{ cm}^{-2} \quad (3)$$

where  $\theta_a$  and  $\theta_b$  are the major and minor axes of the beam (FWHM in arcseconds), respectively,  $T_{\text{ex}}$  is the excitation temperature,  $\tau$  is the optical depth,  $S_{\nu}$  is flux density, and  $dv$  is the velocity interval. Since  $C^{18}O$  is not optically thin in the  $\rho$ -oph A region, the optical depth of the  $C^{18}O$  emission was estimated using the  $C^{18}O$  (2–1) and  $C^{17}O$  (2–1)

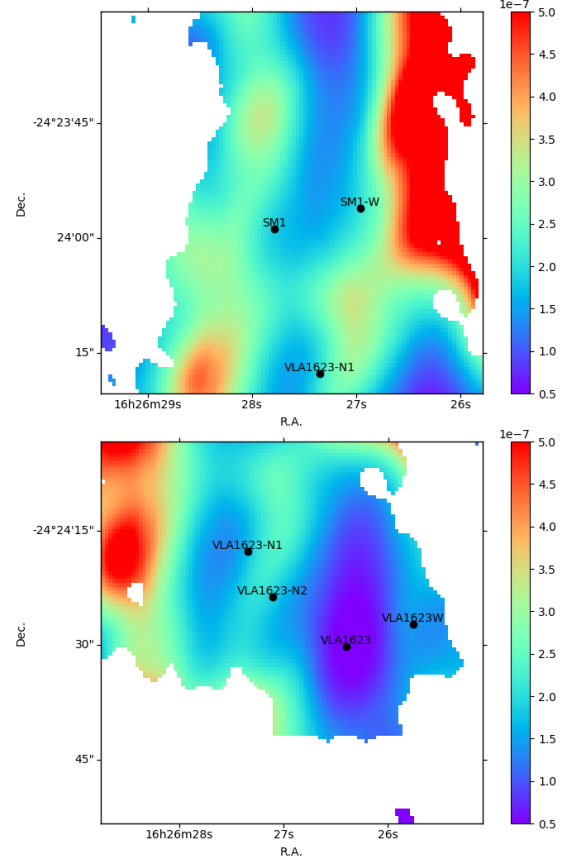


**Figure 8.** Fractional abundance of the  $C^{18}O$  derived from dividing  $N(C^{18}O)$  by  $N(H_2)$ . The color scale ranges from  $2 \times 10^{-8}$  to  $5 \times 10^{-7}$ . The area where continuum emission is below  $3\sigma$  rms noise levels are clipped. The map is restricted to two  $50'' \times 50''$  small regions where optical depths of the  $C^{18}O$  could be calculated.

data observed with the JCMT (Gurney et al. 2008). Unfortunately, the  $C^{17}O$  dataset covers only the  $50'' \times 50''$  areas centered at SM1 and VLA1623. Therefore, we could not derive the optical depth of the  $C^{18}O$  in the SM1N region. We followed the method described in the appendix B of Ladd et al. (1998). The  $^{18}O/^{17}O$  abundance ratio was assumed to be 3.65 (Penzias 1981). Because the JCMT data were sampled in a  $10''$  grid, the optical depth were calculated by interpolating the data points. The calculation showed that  $C^{18}O$  is optically thick in most of the  $\rho$ -Oph A region with the highest value of 5.5 at  $5''$ W of SM1. As for  $N_2H^+$  lines, Di Francesco et al. (2004) showed that the total optical depth of the  $N_2H^+$  line is larger than unity in the  $\rho$ -Oph A region. Therefore, the  $N_2H^+$  column density was calculated from the “isolated” 101-012 component at 93.176265 GHz with optically thin assumption and divided by its relative intensity, which is  $\frac{1}{9}$ . The excitation temperature of the  $C^{18}O$  formula in each pixel was derived from the peak intensity map (Figure 4). The excitation temperature of  $N_2H^+$  was assumed to be 15 K, based on the result of HFS (HyperFine Structure) fitting in Di Francesco et al. (2004). In order to calculate the

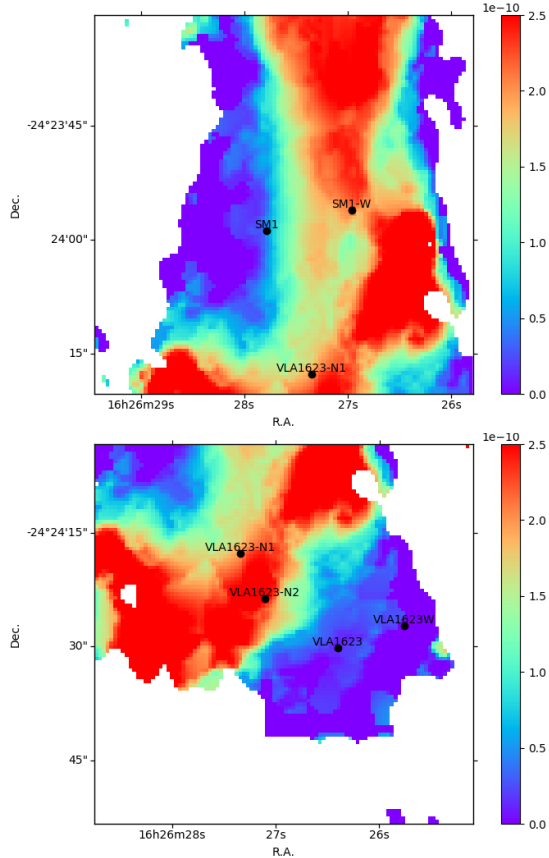


**Figure 9.** Fractional abundance of the  $\text{N}_2\text{H}^+$  derived from dividing  $N(\text{N}_2\text{H}^+)$  by  $N(\text{H}_2)$ . The color scale ranges from 0 to  $1 \times 10^{-10}$ . The area where continuum emission is below  $3\sigma$  rms noise levels are clipped. The areas in the two panels are the same as those of Figure 8.

abundances, the resolution of the  $\text{H}_2$  column density map derived from the continuum data was adjusted to be the same as those of the  $\text{C}^{18}\text{O}$  map and  $\text{N}_2\text{H}^+$  map, respectively. After dividing  $\text{C}^{18}\text{O}$  column density and  $\text{N}_2\text{H}^+$  column density by  $\text{H}_2$  columns density, we derived the abundance distribution over the  $\rho$ -Oph A region.

The  $\text{C}^{18}\text{O}$  abundance distribution in the  $\rho$ -Oph A region is presented in Figure 8 and the  $\text{N}_2\text{H}^+$  abundance distribution in the same region is presented in Figure 9. The column densities of  $\text{H}_2$ ,  $\text{C}^{18}\text{O}$  and  $\text{N}_2\text{H}^+$  and the abundances of  $\text{C}^{18}\text{O}$  and  $\text{N}_2\text{H}^+$  at each source position are listed in Table 2 for comparison. As shown in Figure 8, the  $\text{C}^{18}\text{O}$  abundance decreases significantly at the central N-S ridge and the position of VLA1623. The  $\text{C}^{18}\text{O}$  abundances at those regions are below  $2 \times 10^{-7}$ . On the other hand, the  $\text{C}^{18}\text{O}$  abundance value often used in the interstellar medium is  $1.7\text{--}2 \times 10^{-7}$  (Frerking et al. 1982; Wannier 1980). The higher value of  $4.8 \times 10^{-7}$  is also suggested from the CO abundance of  $2.7 \times 10^{-4}$  (Lacy et al. 1994; Jørgensen et al. 2005) and  $[\text{C}^{18}\text{O}/\text{C}^{16}\text{O}] = 560$  (Wilson & Rood 1994). The  $\text{C}^{18}\text{O}$  abundance values measured in the N-S ridge and VLA1623 are

a factor of 5–10 lower than the interstellar values. On the other hand, the  $\text{C}^{18}\text{O}$  abundance values at SM1, VLA1623-N1, VLA1623-N2, and VLA1623-W are  $\sim 2 \times 10^{-7}$ , which is comparable to that of the interstellar value.

The  $\text{N}_2\text{H}^+$  abundance varies between different sources among  $\rho$ -Oph A. Di Francesco et al. (2004) suggest it is due to different evolutionary stage of each source. The  $\text{N}_2\text{H}^+$  abundance is enhanced in the northern part of the ridge and the C-shaped region including VLA1623-N1 and VLA1623-N2. It drops significantly to the eastern edge of the ridge and the southwestern part including VLA1623. It should be noted that the  $\text{N}_2\text{H}^+$  abundance is very low,  $\sim 1.4 \times 10^{-11}$  at the position of VLA1623, toward which the  $\text{C}^{18}\text{O}$  abundance is also the lowest.

### 3.4. $\text{C}^{17}\text{O}$ , $\text{CH}_3\text{OH}$ and $\text{H}_2\text{CO}$ at SM1

The  $\text{C}^{17}\text{O}$  (2–1), which is typically optically thin, can be used to probe the high-density region near SM1. The optical depth  $\tau$  of  $\text{C}^{17}\text{O}$  in the  $\rho$ -oph A region was obtained from the calculation of the optical depth of  $\text{C}^{18}\text{O}$  in section 3.3. The  $\tau(\text{C}^{17}\text{O})$  has maximum value of 1.5 at  $5''$ W of SM1 and is smaller than unity in most part of the  $\rho$ -oph A region. The integrated intensity map of  $\text{C}^{17}\text{O}$  in the SM1 field is presented in Figure 10a. The  $\text{C}^{17}\text{O}$  emission extends from SM1 through VLA1623-N2, VLA1623-N1, and reaches to VLA1623. The overall distribution of the  $\text{C}^{17}\text{O}$  follows that of the continuum emission. The  $\text{C}^{17}\text{O}$  peak at VLA1623 coincide well with the continuum peak. On the other hand, the  $\text{C}^{17}\text{O}$  peak at SM1 appears at  $\sim 3''$ northeast of the continuum peak. The emission component at  $15''$ NW of SM1 is more than  $17\sigma$ , but there is no counterpart of this component in the continuum or other molecular lines. The missing flux of the  $\text{C}^{17}\text{O}$  was estimated by comparing the flux value of the SMA map convolved to the JCMT beam and that observed with the JCMT. It turned out that the  $\text{C}^{17}\text{O}$  flux recovered by the SMA is only  $\sim 3\%$  of the single-dish flux. This indicates that most of the  $\text{C}^{17}\text{O}$  emission comes from the spatially extended component and very little from the envelope of SM1.

We calculated the  $\text{C}^{17}\text{O}$  abundance from the continuum and  $\text{C}^{17}\text{O}$  data observed with the SMA by following the similar steps described in section 3.3. The  $T_{\text{ex}}$  is assumed to be 27 K. The  $\text{C}^{17}\text{O}$  fractional abundances are  $3.6 \times 10^{-9}$ ,  $2.4 \times 10^{-9}$ ,  $2.4 \times 10^{-9}$  and  $6 \times 10^{-9}$  at VLA1623, SM1, VLA1623-N1 and VLA1623-N2, respectively. After multiplying by the  $^{18}\text{O}/^{17}\text{O}$  relative abundance of 3.65 (Penzias 1981), the derived  $\text{C}^{18}\text{O}$  abundances are  $1.3 \times 10^{-8}$  at VLA1623,  $8.8 \times 10^{-9}$  at SM1 and VLA1623-N1, and  $2.2 \times 10^{-8}$  at VLA1623-N2, which are significantly lower than those estimated in the previous section using the combined  $\text{C}^{18}\text{O}$  and continuum data. Because the abundance values derived here use the SMA data alone, they are the local values at the compact sources. It is likely that the  $\text{C}^{18}\text{O}$  abundance in the compact sources are more than one order of magnitude lower than the interstellar value, even at the positions of SM1, VLA1623-N1, and VLA1623-N2.

The  $\text{CH}_3\text{OH}$  and  $\text{H}_2\text{CO}$  show a localized emission peak at the position of SM1 (Figure 10b and 10c). These line

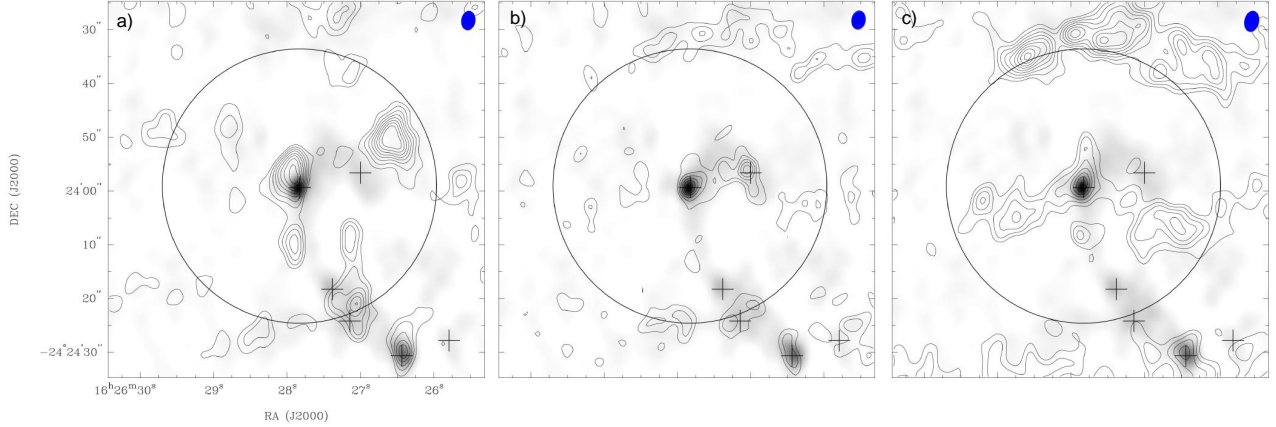


**Figure 10.** Integrated intensity maps of the (a)  $\text{C}^{17}\text{O}$  ( $2-1$ ), (b)  $\text{CH}_3\text{OH}$  ( $5_0-4_0\text{A} + 5_{-1}-4_{-1}\text{E}$ ), and (c)  $\text{H}_2\text{CO}$  ( $3_{1,3}-2_{1,2}$ ) overlaid on the 1.3 mm continuum map shown in the gray scale. Contours are drawn every  $2\sigma$  levels with the lowest contours at  $3\sigma$ . The  $1\sigma$  rms noise level is  $0.11 \text{ Jy beam}^{-1} \text{ km s}^{-1}$  for  $\text{C}^{17}\text{O}$ ,  $0.13 \text{ Jy beam}^{-1} \text{ km s}^{-1}$  for  $\text{CH}_3\text{OH}$ , and  $0.13 \text{ Jy beam}^{-1} \text{ km s}^{-1}$  for  $\text{H}_2\text{CO}$ . The open circle is the field of view of the SMA. The filled ellipse at the top-right corner of each panel is the synthesized beam. The cross signs denote the positions of the continuum peaks.

also show a localized peak toward VLA1623. The  $\text{CH}_3\text{OH}$  shows the secondary peak at SM1-W. The  $\text{CH}_3\text{OH}$  emission is also seen near VLA1623-N2. The spatial distribution of the  $\text{CH}_3\text{OH}$  emission correlate well with that of the continuum emission, except for the missing counterpart of VLA1623-N1. On the other hand, the spatial distribution of the  $\text{H}_2\text{CO}$  is different; the emission extends to the southeast and southwest of SM1. There is no counterpart of VLA1623-N1 and VLA1623-N2 in the  $\text{H}_2\text{CO}$  map. In addition, the  $\text{H}_2\text{CO}$  shows very bright emission at  $30''\text{N}$  of SM1, which corresponds to the northern edge of our field of view. This emission component is also seen in the  $\text{CH}_3\text{OH}$ . The location of these components corresponds to the southern edge of the  $\sim 2.9 \text{ km s}^{-1}$  component seen in the single-dish maps of  $\text{H}_2\text{CO}$  and  $\text{CH}_3\text{OH}$  (Bergman et al. 2011). Since  $\text{CH}_3\text{OH}$  and  $\text{H}_2\text{CO}$  are good tracers for molecular outflow (e.g. Bachiller et al. 2001; Gerin et al. 2015), we searched for the signature of outflow in this region. The  $\text{CH}_3\text{OH}$  and  $\text{H}_2\text{CO}$  emission was separated into the blue-shifted part and red-shifted part (Figure 11). Both blue-shifted and red-shifted components are seen in the vicinity of SM1. However, their spatial distributions do not show clear bipolarity.

## 4. DISCUSSIONS

### 4.1. Nature of the Small condensations

Determining the fate of small condensations such as SM1, VLA1623-N1, -N2 and SM1-W in the dense core will benefit the understanding of low-mass star forming process. The mass of each condensation is derived from the total flux listed in Table 1, using the formula,

$$M_{env} = \frac{SD^2}{\kappa_\nu B_\nu(T_{dust})}, \quad (4)$$

where  $S$  is the total flux,  $D$  is the distance to the source,  $\kappa_\nu$  is the dust mass opacity and  $B_\nu(T_{dust})$  is the Planck function at

a given temperature. The dust mass opacity  $\kappa_\nu$  is assumed to be  $0.005 \text{ cm}^2 \text{ g}^{-1}$ , which is the same as in Motte et al. (1998). The dust temperature is assumed to be 27 K (Andre et al. 1993). The masses of those condensations are in the range of  $10^{-2}-10^{-1} M_\odot$ . For comparison, the mass of the critical Bonnor-Ebert sphere (Bonnar 1956) is calculated from

$$M_{BE} = 2.4 \frac{kT}{mG} r_c, \quad (5)$$

where  $k$  is the Boltzmann constant,  $T$  is the gas kinetic temperature,  $G$  is the gravitational constant,  $m$  is the mean molecular mass, and  $r_c$  is the critical radius. The critical radius  $r_c$  is simply assumed to be the same as the semi major axis of each source. The temperature is assumed to be 27 K, which is the same as that used in the mass calculation. As shown in Table 1, the masses of all the condensations exceed the Bonnor-Ebert mass, which implies those condensations are gravitationally bounded.

VLA1623 and VLA1623W have already been identified as non-coeval multiple system (Murillo & Lai 2013). The recent ALMA observation by Friesen et al. (2014) also found compact structure in SM1. In addition, SM1 is also associated with the source detected in X-ray and radio at 5 GHz (Gagne et al. 2004). These imply that SM1 has already harbored a protostar. VLA1623-N1 has similar properties as SM1. This source is identified as a compact emission source 10 by Kirk et al. (2017) in their 3 mm image observed with the ALMA. In addition, the position of the X-ray source, J162627.4-242418, which is one of the unidentified X-ray sources in Gagne et al. (2004), coincides with that of VLA1623-N1. Recently, Kawabe et al. (2018) studied the properties of SM1 and VLA1623-N1 based on the multi-wavelength observations from radio to X-ray, and proposed that these sources are proto brown dwarfs or in the very early phase of low-mass protostars. On the other hand, there is no clear counterpart of VLA1623-N2 and SM1-W in the ALMA images at 3 mm

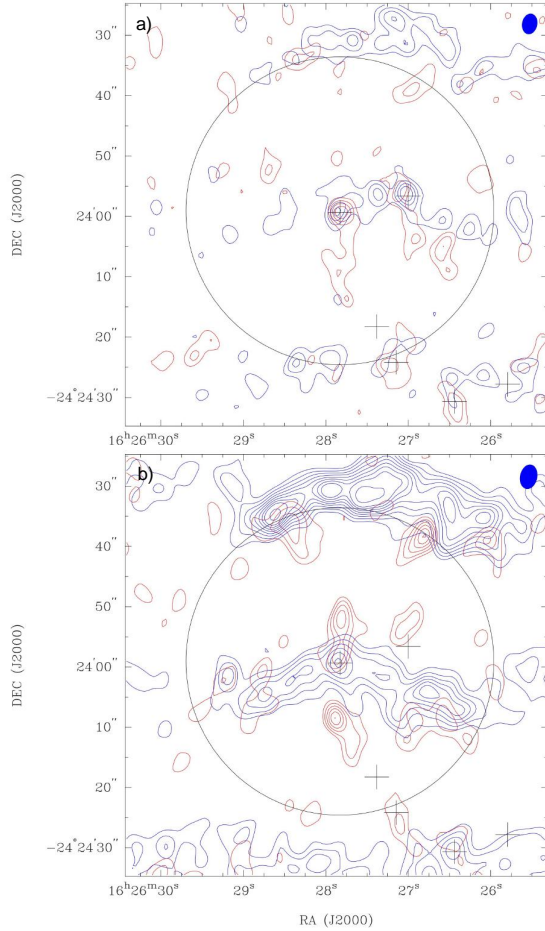


**Figure 11.** (a) Integrated intensity maps of the blue- and redshifted components of the  $\text{CH}_3\text{OH}$  ( $5_0-4_0 \text{ A} + 5_{-1}-4_{-1} \text{ E}$ ) emission. The integrated velocity ranges are  $1.8-3.3 \text{ km s}^{-1}$  (blue) and  $3.5-4.5 \text{ km s}^{-1}$  (red). The contours are every  $2\sigma$  with the lowest contours at  $3\sigma$ . The  $1\sigma$  rms noise levels are  $0.035$  (red) and  $0.042$  (blue)  $\text{Jy beam}^{-1} \text{ km s}^{-1}$ . The ellipse at top right is the beam size of  $3''.3 \times 2''.4$ . (b) Integrated intensity maps of the blue- ( $2-3.5 \text{ km s}^{-1}$ ) and redshifted ( $3.8-5 \text{ km s}^{-1}$ )  $\text{H}_2\text{CO}$  ( $3_{1,3}-2_{1,2}$ ) emission. Contour levels are from  $3\sigma$  in steps of  $2\sigma$ . The  $1\sigma$  rms noise levels are  $0.053$  (red) and  $0.058$  (blue)  $\text{Jy beam}^{-1} \text{ km s}^{-1}$ . The beam size is  $4''.0 \times 2''.7$ .

(Kirk et al. 2017) and  $1.3 \text{ mm}$  (Kawabe et al. 2018). The  $3 \text{ mm}$  image of Kirk et al. (2017) shows some hint of faint condensation at the position of VLA1623-N2. In order to search for the counterpart of VLA1623-N2, we have examined the  $3 \text{ mm}$  continuum image that was made of two datasets available from the ALMA data archive. The resulting image (Figure 12 in Appendix A) has higher sensitivity and resolution than those of the  $3 \text{ mm}$  image in Kirk et al. (2017). However, our new  $3 \text{ mm}$  image does not show clear evidence of compact source at the position of VLA1623-N2. The  $1.3 \text{ mm}$  image presented in Kawabe et al. (2018) also does not show the corresponding source. In addition, there is no counterpart of this source in the X-ray (Gagne et al. 2004) nor in the radio

(Leous et al. 1991; Gagne et al. 2004). Although the water maser source is found at R.A.(J2000) =  $16^{\text{h}}26^{\text{m}}27.028^{\text{s}}$  and Dec. (J2000) =  $-24^{\circ}24'24.284''$  (Yu & Chernin 1997), which is only  $1.6''$  W of VLA1623-N2, it is unlikely that VLA1623-N2 harbor a protostar. Another condensation SM1-W does not have a clear counterpart in the ALMA images of  $3 \text{ mm}$  (Kirk et al. 2017),  $1.3 \text{ mm}$  (Kawabe et al. 2018), and  $0.84 \text{ mm}$  (Friesen et al. 2014) as well. This source is not detected in the X-ray (Gagne et al. 2004) nor in the radio (Leous et al. 1991; Gagne et al. 2004). The absence of compact condensation implies that VLA1623-N2 and SM1-W are still in the prestellar stage.

#### 4.2. Physical condition and CO depletion

As shown in Figure 4, the peak intensity of the  $\text{C}^{18}\text{O}$  is enhanced to  $T \sim 40-50 \text{ K}$  at the edges of the  $\rho$ -Oph A ridge, while it is lower than  $30 \text{ K}$  toward the center of the ridge. The higher temperature in the edges is likely due to external heating by stellar UV and X-ray photons. One of the possible heating sources is Source 1 (hereafter Oph S1) at  $\sim 1.5'$  ( $12,000 \text{ au}$ ) E of SM1N. Oph S1 having a luminosity of  $\sim 1600 L_{\odot}$  (Wilking et al. 2005) is known to be a binary with a B4 primary and companion with a K magnitude of 8.3 (Simon et al. 1995), and is emitting both strong non-thermal radio and X-ray emission (Gagne et al. 2004). The UV as well as higher energy photons reach the eastern surface of the  $\rho$ -Oph A ridge and heat the eastern edge of the ridge. Another heating source is the B2 star HD147889 with  $\sim 4500 L_{\odot}$  (Greene & Young 1989), which is  $\sim 15'$  ( $0.5 \text{ pc}$ ) to the southwest and behind the  $\rho$ -Oph A ridge (Liseau et al. 1999). This source is likely to be responsible in heating the ridge from the west. Since the continuum emission from mid-infrared, far-infrared, to millimeter in the  $\rho$ -Oph A region is modeled well with the external heating of S1 and HD147889 (Liseau et al. 2015), it is natural to consider that the molecular gas in the  $\rho$ -Oph A ridge is also heated from these two stars.

On the other hand, the  $\text{C}^{18}\text{O}$  intensity drops significantly toward the continuum ridge; especially, it is below  $15 \text{ K}$  in the region between SM1 and SM1N. In this region, the abundances of the  $\text{C}^{18}\text{O}$  and  $\text{N}_2\text{H}^+$  show clear anti-correlation. Similar anti-correlation between  $\text{C}^{18}\text{O}$  ( $3-2$ ) and  $\text{N}_2\text{H}^+$  ( $3-2$ ) is also seen in Liseau et al. (2015). These imply that the gas temperature in the center of the  $\rho$ -Oph A ridge, where the external radiation is shielded, is lower than the CO freeze-out temperature of  $\sim 25 \text{ K}$  (Öberg et al. 2005). In the cold and dense environment,  $\text{N}_2$ , a parent molecule of  $\text{N}_2\text{H}^+$ , is also expected to freeze-out. Since the desorption energy ratio of  $\text{N}_2$  and CO measured in the recent laboratory experiments is  $\sim 0.9$  (Öberg et al. 2005; Fayolle et al. 2016), the  $\text{N}_2$  freeze-out temperature is only a few degrees lower than that of CO. The clear anti-correlation between  $\text{C}^{18}\text{O}$  and  $\text{N}_2\text{H}^+$  implies that sufficient amount of  $\text{N}_2$  is in the gas-phase. This is probably because that the area with the  $\text{C}^{18}\text{O}-\text{N}_2\text{H}^+$  anti-correlation is still starless (Kirk et al. 2017) and the freeze-out timescales of molecules are long enough to differentiate the gas-phase abundance of CO and  $\text{N}_2$ . As a result, the

$\text{N}_2\text{H}^+$  abundance increases after CO, which is the main destructor of  $\text{N}_2\text{H}^+$ , disappears. SM1 is located at the eastern edge of the  $\text{C}^{18}\text{O}$  depletion zone. Although the  $\text{C}^{18}\text{O}$  abundance at the position of SM1 derived from the combined maps of the continuum and  $\text{C}^{18}\text{O}$ ,  $1.9 \times 10^{-7}$ , is not very low as compared to the interstellar value of  $1.7\text{--}4.8 \times 10^{-7}$ , this is because of the spatially extended emission along the line of sight. The  $\text{C}^{18}\text{O}$  abundance at SM1 is a factor of 20 lower if it is derived from the SMA data. This suggests that the CO depletion is also significant in the dense gas envelope of SM1. The  $\text{C}^{18}\text{O}$  abundance shows the lowest value of  $4.3 \times 10^{-8}$  toward VLA1623. Although the  $\text{C}^{18}\text{O}$  line traces the rotating disk around VLA1623A, there is no  $\text{C}^{18}\text{O}$  emission from VLA1623B and the envelope surrounding this binary system (Murillo & Lai 2013; Murillo et al. 2013). This implies that most of the dense gas surrounding the VLA1623A&B binary system is colder than the CO freeze-out temperature. Interestingly, the  $\text{N}_2\text{H}^+$  also shows the lowest abundance at VLA1623. This implies that the temperature of the dense gas surrounding VLA1623 is lower than the freeze-out temperature of  $\text{N}_2$ . Once both CO and  $\text{N}_2$  freeze-out completely, the  $\text{N}_2\text{H}^+$  abundance does not increase when the gas is heated by the newly born star. Since the desorption energy of  $\text{N}_2$  does not differ significantly from that of CO, the  $\text{N}_2$  desorption area is expected to be comparable to the CO desorption area. In such a case,  $\text{N}_2\text{H}^+$  is easily destroyed by the CO desorbed from grains, and cannot have enough abundance to be observed.

Molecular clouds irradiated externally by nearby stars are often found in high-mass star forming regions. For example, molecular gas in the S255-S257 system is located between two HII regions, S255 and S257, and forms an elongated ridge compressed and illuminated by two HII regions (Minier et al. 2006). The dense gas ridge of this system harbors a cluster of YSOs with more than one hundred members (Ojha et al. 2011). The morphology of molecular ridge and the spatial distribution of the YSOs suggest that the star formation activity in this system is induced by the compression from two HII regions. On the other hand, dense molecular ridge irradiated by two early type stars in both sides is barely seen in the low-mass star forming regions;  $\rho$ -Oph A is almost a unique example. In the case of  $\rho$ -Oph A, the effect of external sources is moderate. Molecular gas is interacting with the Photon Dominated Region (PDR) around the nearest star S1. The HII region around this star has a diameter of  $<20''$  (Andre et al. 1988), which is much smaller than the size of the PDR. The curved ridge morphology observed in the  $\text{C}^{18}\text{O}$  (3–2) follows the outer edge of the spherical shell of the PDR around S1 traced by  $\text{H}_2$ , [OI] (Larsson & Liseau 2017), and [CII] (Mookerjee et al. 2018), suggesting that the molecular ridge has been compressed by the PDR. However, our  $\text{C}^{18}\text{O}$  (2–1) data do not show the kinematical signature of external compression.

## 5. CONCLUSIONS

We have studied the physical and chemical conditions of the  $\rho$ -Oph A region using the 1.3 mm continuum, and molec-

ular lines such as  $\text{C}^{18}\text{O}$  (2–1) and  $\text{N}_2\text{H}^+$  (1–0). The 1.3 mm continuum and  $\text{C}^{18}\text{O}$  (2–1) data observed with the SMA were combined with the data obtained with the IRAM 30 m telescope and JCMT, respectively, in order to fill the short-spacing information. Our main conclusions are summarized as follows.

1. The combined 1.3 mm map reveals that the three major sources, VLA1623, SM1, and SM1N are embedded in the extended emission running along the north-south direction. VLA1623 and SM1 contain the spatially compact components, while SM1N does not have a compact component. The continuum emission around the SM1 peak is extended toward the northwest direction. The secondary peak, SM1-W, to the west of the SM1 peak implies the presence of small-scale clumps. However, the location of SM1-W does not coincide with those of the clumps reported in Nakamura et al. (2012).
2. In addition to VLA1623 and SM1, two compact condensations, VLA1623-N1 and VLA1623-N2, are identified in the continuum ridge connecting VLA1623 and SM1. In addition, VLA1623W is also identified as a separate peak. All of the small condensations identified in the  $\rho$ -Oph A region are gravitationally bounded. Among the newly discovered small condensations, VLA1623-N1 has a X-ray counterpart and is likely to harbor a young stellar object. On the other hand, VLA1623-N2 and SM1-W are starless.
3. The spatial distribution of the  $\text{C}^{18}\text{O}$  is significantly different from that of the continuum; the  $\text{C}^{18}\text{O}$  emission is enhanced at the eastern and western edges of the continuum ridge. The brightness temperature of the  $\text{C}^{18}\text{O}$  line is enhanced to 40–50 K in the eastern and western edges. This is consistent with the picture that the gas in the  $\rho$ -Oph A ridge is heated externally by the nearby B-stars Oph S1 and HD147889.
4. On the other hand, the gas in the inner dense ridge remains cold. The  $\text{C}^{18}\text{O}$  intensity drops below 15 K in the region between SM1 and SM1N. In this region, the  $\text{C}^{18}\text{O}$  abundance decreases and shows clear anti-correlation with the  $\text{N}_2\text{H}^+$  abundance.
5. Both  $\text{C}^{18}\text{O}$  and  $\text{N}_2\text{H}^+$  abundances decrease significantly toward the Class 0 protostar VLA1623. This implies that most of the dense gas surrounding VLA1623 is colder than the freeze-out temperature of  $\text{N}_2$ , which is a few degrees lower than that of CO.
6. The velocity structure of  $\text{C}^{18}\text{O}$  suggests that the  $\rho$ -oph A ridge consists of three components with different systemic velocities. These three velocity components are known to have different chemical properties; the northern component at  $3.1 \text{ km s}^{-1}$  is deficient in deuterated species, the southern component at  $3.7 \text{ km s}^{-1}$  is rich in deuterated species, and the north-western

component at  $2.9 \text{ km s}^{-1}$  shows high abundance in methanol (Bergman et al. 2011; Garay et al. 2002).

7. The  $\text{CH}_3\text{OH}$  shows the blue-shifted and red-shifted components in the vicinity of SM1. These components are likely to trace the outflow activity of the embedded protostar in SM1. The similar components are also seen in the  $\text{H}_2\text{CO}$ . However, the spatially extended  $\text{H}_2\text{CO}$  emission does not show clear bipolarity.

We thank James Di Francesco for providing the  $\text{N}_2\text{H}^+$  data cube obtained with the IRAM 30 m telescope and the BIMA interferometer, and 1.3 mm continuum data observed with the IRAM 30 m telescope. We thank all the SMA staff in Hawaii, Cambridge, and Taipei for their kind help during the observations. We thank the anonymous referee for the constructive suggestions. The Submillimeter Array is a joint project between the Smithsonian Astrophysical Observatory and the Academia Sinica Institute of Astronomy and Astrophysics and is funded by the Smithsonian Institution and the Academia Sinica (Ho et al. 2004). The James Clerk Maxwell

Telescope has historically been operated by the Joint Astronomy Centre on behalf of the Science and Technology Facilities Council of the United Kingdom, the National Research Council of Canada and the Netherlands Organisation for Scientific Research. This paper makes use of the following ALMA data: ADS/JAO.ALMA#2013.1.00187.S, ADS/JAO.ALMA#2016.1.01468.S. ALMA is a partnership of ESO (representing its member states), NSF (USA) and NINS (Japan), together with NRC (Canada), MOST and ASIAA (Taiwan), and KASI (Republic of Korea), in cooperation with the Republic of Chile. The Joint ALMA Observatory is operated by ESO, AUI/NAOJ and NAOJ. The National Radio Astronomy Observatory is a facility of the National Science Foundation operated under cooperative agreement by Associated Universities, Inc. N.H. acknowledges a grant from the Ministry of Science and Technology (MoST) of Taiwan (MoST 107-2119-M-001-029)

*Facilities:* SMA, IRAM:30m, JCMT, ALMA

*Software:* MIR (<https://github.com/qi-molecules/sma-mir>), MIRIAD (Sault et al. 1996), Astropy (The Astropy Collaboration 2013, 2018), Starlink (Currie et al. 2014), CASA (McMullin et al. 2007)

## APPENDIX

### A. THE 3 MM ALMA CONTINUUM MAP OF THE $\rho$ -OPH A RIDGE

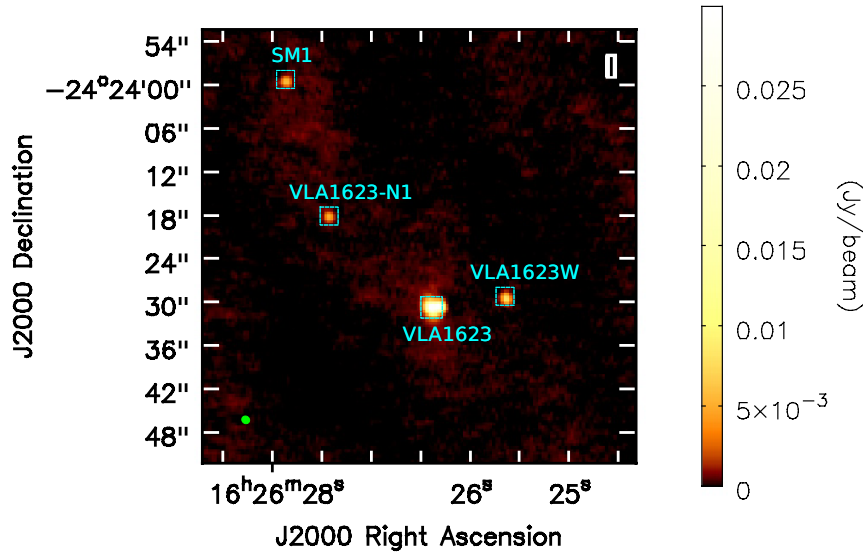


**Figure 12.** 3 mm Continuum map obtained by combining two ALMA datasets. The  $1\sigma$  rms noise level is  $0.18 \text{ mJy beam}^{-1}$ . The green ellipse at bottom left corner denotes the synthesized beam size of  $1''.1 \times 1''.0$ .

In Figure 12, we present the 3mm continuum map of the  $\rho$ -oph A ridge, which is made by combining ALMA data from two projects (Project code = 2013.1.00187.S and 2016.1.01468.S). The ALMA datasets were obtained from ALMA Science Archive. The first Band 3 observations from project 2013.1.00187.S were made during cycle 2 on January 31, 2015. The array consisted of 37 antennas with relatively compact configuration. The field center is at the position of VLA1623. The continuum data were obtained at 101, 103, and 113 GHz, each covering a bandwidth of 2GHz. The total integration time is 60.48 seconds. The detail of the observation is also described in Kirk et al. (2017).

The second Band 3 observations from project 2016.1.01468.S were made during cycle 4 on November 16, 2016. The array was in C40-4 configuration. The field is also centered at the position of VLA1623. The observation covers frequency range from 108.72 GHz to 110.94 GHz. The total integration time is 241.92 seconds

CASA (McMullin et al. 2007) was used to calibrate and reduce both datasets. We concatenated two calibrated datasets and used “tclean” in the mfs (multi-frequency synthesis) mode to generate the combined 3 mm continuum map. The robust weighting of 0.5 was adopted, providing the synthesized beam size of  $1''.1 \times 1''.0$ . The rms noise level of the 3 mm continuum image is  $0.18 \text{ mJy beam}^{-1}$ .

## REFERENCES

- Andre, P., Montmerle, T., Feigelson, E. D., Stine, P. C., & Klein, K.-I. 1988, *ApJ*, 335, 940
- Andre, P., Ward-Thompson, D., & Barsony, M. 1993, *ApJ*, 406, 122
- Bachiller, R., Pérez Gutiérrez, M., Kumar, M. S. N., & Tafalla, M. 2001, *A&A*, 372, 899
- Bergman, P., Parise, B., Liseau, R., & Larsson, B. 2011, *A&A*, 527, A39
- Bonnar, W. B. 1956, *MNRAS*, 116, 351
- Cavanagh, B., Jenness, T., Economou, F., & Currie, M. 2008, *AN*, 329, 295
- Chen, X., Arce, H. G., Zhang, Q., et al. 2013, *ApJ*, 768, 110
- Currie, M. J., Berry, D. S., & Jenness et al., T. 2014, in *Astronomical Data Analysis Software and Systems XXIII*, Vol. 485, 391
- Di Francesco, J., Andre, P., & Myers, P. C. 2004, *ApJ*, 617, 425
- Fayolle, E. C., Balfe, J., Loomis, R., et al. 2016, *ApJ*, 816, L28
- Frerking, M. A., Langer, W. D., & Wilson, R. W. 1982, *ApJ*, 262, 590
- Friesen, R. K., Di Francesco, J., Bourke, T. L., et al. 2014, *ApJ*, 797, 27
- Gagne, M., Skinner, S. L., & Daniel, K. J. 2004, *ApJ*, 613, 393
- Garay, G., Mardones, D., Rodríguez, L. F., Caselli, P., & Bourke, T. L. 2002, *ApJ*, 567, 980
- Gerin, M., Pety, J., Fuente, A., et al. 2015, *A&A*, 577, L2
- Greene, T. P., & Young, E. T. 1989, *ApJ*, 339, 258
- Gurney, M., Plume, R., & Johnstone, D. 2008, *PASP*, 120, 1193
- Ho, P. T. P., Moran, J. M., & Lo, K. Y. 2004, *ApJ*, 616, L1
- Johnstone, D., Wilson, C. D., Moriarty-Schieven, G., et al. 2000, *ApJ*, 545, 327
- Jørgensen, J. K., Schöier, F. L., & van Dishoeck, E. F. 2005, *A&A*, 435, 177
- Kawabe, R., Hara, C., Nakamura, F., et al. 2018, arXiv:1810.00573
- Kirk, H., Dunham, M. M., Francesco, J. D., et al. 2017, *ApJ*, 838, 114
- Lacy, J. H., Knacke, R., Geballe, T. R., & Tokunaga, A. T. 1994, *ApJ*, 428, L69
- Ladd, E. F., Fuller, G. A., & Deane, J. R. 1998, *ApJ*, 495, 871
- Larsson, B., & Liseau, R. 2017, *A&A*, 608, A133
- Leous, J. A., Feigelson, E. D., Andre, P., & Montmerle, T. 1991, *ApJ*, 379, 683
- Liseau, R., Larsson, B., Bergman, P., et al. 2010, *A&A*, 510, A98
- Liseau, R., White, G. J., Larsson, B., et al. 1999, *A&A*, 344, 342
- Liseau, R., Larsson, B., Lunttila, T., et al. 2015, *A&A*, 578, A131
- Loren, R. B., Wootten, A., & Wilking, B. A. 1990, *ApJ*, 365, 269
- Mangum, J. G., & Shirley, Y. L. 2015, *PASP*, 127, 266
- McMullin, J. P., Waters, B., Schiebel, D., Young, W., & Golap, K. 2007, in *Astronomical Data Analysis Software and Systems XVI*, Vol. 376, 127
- Mezger, P., Sievers, A., Zylka, R., et al. 1992, *A&A*, 265, 743
- Minier, V., Peretto, N., Longmore, S. N., et al. 2006, *Proceedings of the International Astronomical Union*, 2, 160
- Mookerjee, B., Sandell, G., Vacca, W., Chambers, E., & Güsten, R. 2018, *A&A*, 616, A31
- Motte, F., Andre, P., & Neri, R. 1998, *A&A*, 336, 150
- Murillo, N. M., & Lai, S.-P. 2013, *ApJ*, 764, L15
- Murillo, N. M., Lai, S.-P., Bruderer, S., Harsono, D., & van Dishoeck, E. F. 2013, *A&A*, 560, A103
- Nakamura, F., Takakuwa, S., & Kawabe, R. 2012, *ApJ*, 758, L25
- Öberg, K. I., van Broekhuizen, F., Fraser, H. J., et al. 2005, *ApJ*, 621, L33
- Ojha, D. K., Samal, M. R., Pandey, A. K., et al. 2011, *ApJ*, 738, 156
- Ortiz-León, G. N., Loinard, L., Kounkel, M. A., et al. 2017, *ApJ*, 834, 141
- Penzias, A. A. 1981, *ApJ*, 249, 518
- Sault, R. J., Staveley-Smith, L., & Brouw, W. N. 1996, *A&AS*, 120, 375
- Shu, F. H., Adams, F. C., & Lizano, S. 1987, *ARA&A*, 25, 23
- Simon, M., Ghez, A. M., Leinert, C., et al. 1995, *ApJ*, 443, 625
- Takakuwa, S. 2003, *NRO Technical Report*, No.65
- Vogel, S. N., Wright, M. C. H., Plambeck, R. L., & Welch, W. J. 1984, *ApJ*, 283, 655
- Wannier, P. G. 1980, *ARA&A*, 18, 399
- White, G. J., Drabek-Maunder, E., Rosolowsky, E., et al. 2015, *MNRAS*, 447, 1996
- Wilking, B. A., Meyer, M. R., Robinson, J. G., & Greene, T. P. 2005, *AJ*, 130, 1733
- Wilson, C. D., Avery, L. W., Fich, M., et al. 1999, *ApJ*, 513, L139
- Yu, T., & Chernin, L. M. 1997, *ApJ*, 479, L63